

Estimating Mean Scatterer Spacing with the Frequency-Smoothed Spectral Autocorrelation Function

Tommy Varghese, *Student Member, IEEE*, and Kevin D. Donohue, *Member, IEEE*

Abstract— The quasiperiodicity of regularly spaced scatterers results in characteristic patterns in the spectra of backscattered ultrasonic signals from which the mean scatterer spacing can be estimated. The mean spacing has been considered for classifying certain biological tissue. This paper addresses the problem of estimating the mean scatterer spacing from backscattered ultrasound signals using the frequency-smoothed spectral autocorrelation (SAC) function. The SAC function exploits characteristic differences between the phase spectrum of the resolvable quasi-periodic scatterers and the unresolvable uniformly distributed (diffuse) scatterers to improve estimator performance over other estimators that operate directly on the magnitude spectrum. Mean scatterer spacing estimates are compared for the frequency-smoothed SAC function and a cepstral technique using an AR model. Simulation results indicate that SAC-based estimates converge more reliably over smaller amounts of data than cepstrum-based estimates. An example of computing an estimate from liver tissue scans is also presented for the SAC function and the AR cepstrum.

I. INTRODUCTION

THE backscattered ultrasound rf signal provides information on many characteristics of the scatterer structure in tissue. However, the simultaneous occurrence of various phenomena like frequency dependent attenuation, different types of scattering, and diffraction makes it difficult to extract information related to a single tissue parameter. This paper presents a method for estimating the mean scatterer spacing in tissue where two types of scattering structures exist, regular (resolvable) and diffuse (unresolvable). The resolvable regular scatterers are quasi-periodic scatterers separated by at least one resolution cell. Scattering of this nature has been observed in liver tissue, where the lobular structure of the liver and the portal triads contribute to the resolvable regular scattering with a mean spacing near 1 mm, while the speckle or diffuse scattering is generated from the many randomly distributed scatterers within the resolution cell [1]–[5]. The method described in this paper is shown to provide more reliable estimates in the presence of strong diffuse scattering than methods that primarily use the magnitude of the spectrum.

Manuscript received July 25, 1994; revised November 15, 1994; accepted November 16, 1994. This material is based on work supported in part by the National Cancer Institute and National Institutes of Health, Grant CA52823.

The authors are with the Department of Electrical Engineering University of Kentucky Lexington, KY 40503 USA.

IEEE Log Number 9409994.

Mean scatterer spacing has been used by various investigators for tissue characterization. Fellingham and Sommer used this parameter to differentiate between normal and cirrhotic liver, and to distinguish normal spleen tissue from those with lymphoma [2]. Garra *et al.* used this parameter in a multi-feature classification of diffuse liver disease [3]. Wagner *et al.* used mean scatterer spacing in conjunction with the ratio of regular-to-diffuse scatterer intensities, and the fractional standard deviation in the regular scatterers to classify tissue architecture [4], [5]. Landini and Verrazzani classified normal and diseased tissue based on the mean and variance estimates of the scatterer spacing using a Gamma distribution [6].

Spectral techniques for estimating the mean scatterer spacing can be classified into power spectrum methods (PSD) [2], cepstral methods [6]–[8], and spectral redundancy techniques [10]–[13]. Mean scatterer spacing has also been estimated from intensity (squared magnitude) scans using a weighted thresholding procedure [4], [5]. The cepstral methods are attractive because they provide a means to reduce the distortion and interference due to system effects in the spectrum of the received A-scan. The cepstrum, which is the Fourier transform of the logarithm of the PSD, converts the multiplicative relationship between the scatterer function and the system response in the Fourier domain to an additive one. Cepstral techniques successfully separate the scatterer function from the system response when the PSD of the system response is a slowly varying component relative to the effect of the regular scatterers. Therefore, by finding a cutoff point along the cepstral axis to reject most of the energy due to the system response (low frequency), the remaining signal is primarily due to the regular scatterers (high frequency). Thus, beyond the cutoff point the location of the largest peak in the cepstrum corresponds to the mean scatterer spacing. Wear *et al.* [8] proposed the use of cepstral techniques using an AR spectral estimator (based on the Burg's algorithm). For phantom data (containing regularly spaced scatterers) this algorithm performed considerably better than cepstral methods using the periodogram especially when smaller gate lengths were used.

Spectral redundancy, characterized by the time-averaged SAC function, has also been used to estimate the mean scatterer spacing in ultrasound A-scans [10]–[13]. It was shown in [12] that the mean scatterer spacing estimates obtained using the time-averaged SAC function converge to the true value

of the scatterer spacing over smaller lengths of data when compared to cepstral techniques using the periodogram. In addition, spacing estimates obtained using the SAC function converge to the correct value of the scatterer spacing (no bias) for quasiperiodic scatterers in the presence of a strong diffuse component.

This paper introduces a frequency-smoothing technique to obtain a statistical SAC function. Mean scatterer spacing estimators using the frequency-smoothed SAC function are compared to a cepstral technique using an AR-model. A brief description of the mean scatterer spacing estimators are discussed in Section II. Section III discusses the simulation experiment and analyzes the relative merits of the techniques used in determining the scatterer spacing. The SAC function and AR cepstrum estimates obtained from *in vivo* data from liver tissue are presented in Section IV. Finally, Section V summarizes the significance of the results for ultrasonic tissue characterization.

II. THEORY

The tissue structure is modeled as a sparse collection of randomly-distributed weak scattering particles that interact with the incident pulse as it propagates through the tissue. The scattering particles are assumed to interact with the pulse only once. The scattering function for the regular and diffuse scatterers within the beam field of the ultrasound pulse can be written as

$$x(t) = \sum_{n=1}^{N_S} a_n(t - \tau_n) + \sum_{n=1}^{N_D} v_n(t - \theta_n) \quad (1)$$

where t is a time axis (related to the radial distance by the velocity of the pulse), N_D is the total number of diffuse scatterers, v_n denotes the scattering function of the n^{th} diffuse scatterer with delay θ_n corresponding to its effective scattering center, N_S is the total number of regular scatterers, a_n denotes the scattering function of the n^{th} regular scatterer with delay τ_n corresponding to its effective scattering center.

Attenuation of the propagating ultrasound pulse depends on the scattering and absorption properties of the tissue. The system response due to the propagation of the pulse is represented by a time varying function $h(t, \tau)$, which accounts for the frequency dependent attenuation of the pulse as it propagates through the tissue. The backscattered energy produced by the interaction of the pulse with the scattering particles (A-scan) can now be written as

$$y(\tau) = \sum_{n=1}^{N_S} \int_{-\infty}^{\infty} h(\tau_n, \tau - \lambda) a_n(\lambda - \tau_n) d\lambda + \sum_{n=1}^{N_D} \int_{-\infty}^{\infty} h(\theta_n, \tau - \lambda) v_n(\lambda - \theta_n) d\lambda \quad (2)$$

where λ is the variable of integration for the convolution integral. The Fourier transform of (2) with respect to τ , can

be written as

$$Y(f) = \sum_{n=1}^{N_S} H(\tau_n, f) A_n(f) e^{-j2\pi f \tau_n} + \sum_{n=1}^{N_D} H(\theta_n, f) V_n(f) e^{-j2\pi f \theta_n}. \quad (3)$$

Now if $H(\cdot, f)$ does not change significantly over a neighborhood of several resolution cells about t (negligible attenuation), the Fourier transform at a given time t , can be written as

$$Y(f; t) = H(f; t) \left(\sum_{n=1}^{N_S} A_n(f) e^{-j2\pi f \tau_n} + \sum_{n=1}^{N_D} V_n(f) e^{-j2\pi f \theta_n} \right) \quad (4)$$

where $H(f; t)$ and $Y(f; t)$ are the Fourier transforms of $h(t, \tau)$ and $y(t, \tau)$ over a local neighborhood of t , respectively, and $A_n(f)$ and $V_n(f)$ denote the complex frequency dependent scattering strength associated with the scatterer functions $a_n(\tau)$ and $v_n(\tau)$, respectively.

A. The Spectral Autocorrelation Function

The SAC function of a local A-scan segment is defined over a bifrequency plane by

$$S(f_1, f_2; t) = E[Y(f_1; t) Y^*(f_2; t)]. \quad (5)$$

where $Y(\cdot)$ is the Fourier transform of the windowed A-scan segment centered at t , and $Y^*(\cdot)$ is its complex conjugate. Note that unlike the PSD, which is real valued and only represents the correlation between the same frequency components, the SAC function is complex and represents the correlation between different frequency components for $f_1 \neq f_2$. The diagonal in the bifrequency plane of the SAC function, defined by $f_1 = f_2$, is equivalent to the PSD.

Contributions from the diffuse component add directly to the PSD, while the expected value for the diffuse component is zero for the off-diagonal SAC components, as was shown by Varghese and Donohue in [12] for the time-averaged SAC function. As a result, in the presence of diffuse scatterers the SAC function provides a more robust estimate of the scatterer spacing relative to cepstral estimates that use the PSD characterization of the signal. An alternative method to time averaging the SAC function to improve reliability, is frequency averaging or frequency smoothing. Frequency smoothing can be applied to single data segments that include several scatterers (at least 3 for consistent performance). Time-averaging, on the other hand requires several data segments (where each segment must contain 3 or more scatterers) before a reliable statistical spectrum is obtained. Frequency smoothing also has the advantage that no phase alignment is required to maintain the coherent phase between segments as must be done with time-averaging [12].

The frequency-smoothed SAC function computed from a data segment of duration Δt centered at t , can be expressed as

$$S_{\Delta t}(f_1, f_2; t) \simeq [Y_{\Delta t}(f_1; t) Y_{\Delta t}^*(f_2; t)] \otimes G_{1/\Delta f}(f_1, f_2) \quad (6)$$

where $G_{1/\Delta f}(\cdot)$ represents the frequency-smoothing kernel of effective duration Δf along both the f_1 and f_2 axis, and \otimes denotes convolution. The relationship between the SAC function and the scatterer configurations is seen by substituting in $Y(\cdot)$ from (4) into (5):

$$S(f_1, f_2; t) = H(f_1; t)H^*(f_2; t) \times E \left[\sum_{n=1}^{N_S} \sum_{m=1}^{N_S} A_n(f_1)A_m^*(f_2)e^{-j2\pi(f_1\tau_n - f_2\tau_m)} + \sum_{n=1}^{N_S} \sum_{m=1}^{N_D} A_n(f_1)V_m^*(f_2)e^{-j2\pi(f_1\tau_n - f_2\theta_m)} + \sum_{n=1}^{N_D} \sum_{m=1}^{N_S} V_n(f_1)A_m^*(f_2)e^{-j2\pi(f_1\theta_n - f_2\tau_m)} + \sum_{n=1}^{N_D} \sum_{m=1}^{N_D} V_n(f_1)V_m^*(f_2)e^{-j2\pi(f_1\theta_n - f_2\theta_m)} \right] \quad (7)$$

The above expression can be simplified under general assumptions for the diffuse scatterers. These assumptions are, that the diffuse scatterer positions are uniformly distributed over the A-scan segment, the values of their scattering functions are uncorrelated with each other and their positions, and their positions are uncorrelated with the regular scatterer positions. The assumption of uniformly distributed diffuse scatterers leads to an expected value of zero for the diffuse scattering process (i.e. $E[e^{-j2\pi f\theta_n}] = 0$, when θ_n is uniformly distributed between $(-1/2, 1/2)$). The assumption of uniformly distributed scatterers further leads to a scattering process which is wide-sense-stationary (WSS) and uncorrelated [19]. Under the assumption that the diffuse scatterers are uncorrelated with the positions of the regular scatterers, the expected value of the summation cross-product terms between the diffuse and regular scatterers (second and third double summations in (7)) reduces to zero. Since the diffuse scatterer positions are uncorrelated with each other, terms corresponding to different

scatterers in the last double summation of (7) become zero (i.e. $E[V_n(f_1)V_m^*(f_2)e^{-j2\pi(f_1\theta_n - f_2\theta_m)}] = 0$, $m \neq n$). In addition, since the diffuse scatterer process is WSS over the region of interest, the terms where $f_1 \neq f_2$ in the last double summation term are uncorrelated [19]. Thus, the diffuse scattering process contributes only to the diagonal elements of the SAC function, and (7) can be rewritten as

$$S(f_1, f_2; t) = H(f_1; t)H^*(f_2; t) \times \left(E \left[\sum_{n=1}^{N_S} \sum_{m=1}^{N_S} A_n(f_1)A_m^*(f_2)e^{-j2\pi(f_1\tau_n - f_2\tau_m)} \right] + \sum_{n=1}^{N_D} E[V_n(f_1)V_n^*(f_2)]\delta(f_1 - f_2) \right) \quad (8)$$

where $\delta(f_1 - f_2)$ is the Kronecker delta function. The result in (8) is based on the previous assumptions of uncorrelatedness for the diffuse scatterers only.

Since the critical information for determining scatterer spacing is related to the difference between two correlated frequencies, (8), will be expressed in terms of $\alpha = f_2 - f_1$, where positive α represents the diagonal components over the upper triangular region of the SAC function (for $\alpha = 0$, we obtain the PSD of the function). Substitute f_2 into (8), and let $f_1 = f$ to obtain (9) shown at the bottom of this page.

The Kronecker delta function in the last summation term of (9) indicates that the expected value of the diffuse component contributes to the SAC function only when $\alpha = 0$, which represents the PSD. For $\alpha \neq 0$, only the regular scattering component remains, and (9) reduces to (10) shown at the bottom of this page.

To further simplify and understand the relationship between SAC function local maxima and scatterer spacing, a variable related to the scatterer spacing is obtained using the substitution $\tau_i = i \Delta_i$, where i represents the number of intervals, and Δ_i is the average spacing for the scatterer up to the i^{th}

$$S(f, f + \alpha; t) = H(f; t)H^*(f + \alpha; t) \times \left(E \left[\sum_{n=1}^{N_S} \sum_{m=1}^{N_S} A_n(f)A_m^*(f + \alpha)e^{-j2\pi f(\tau_n - \tau_m)} e^{j2\pi\alpha\tau_m} \right] + \sum_{n=1}^{N_D} E[V_n(f)V_n^*(f + \alpha)]\delta(\alpha) \right) \quad (9)$$

$$S(f, f + \alpha; t) = H(f; t)H^*(f + \alpha; t)E \left[\sum_{n=1}^{N_S} \sum_{m=1}^{N_S} A_n(f)A_m^*(f + \alpha)e^{-j2\pi f(\tau_n - \tau_m)} e^{j2\pi\alpha\tau_m} \right] \quad (10)$$

$$S(f, f + \alpha; t) = H(f; t)H^*(f + \alpha; t)E \left[\sum_{n=1}^{N_S} \sum_{m=1}^{N_S} A_n(f)A_m^*(f + \alpha)e^{-j2\pi f\Delta(n-m)} e^{j2\pi\alpha\Delta m} \right] \quad (11)$$

scatterer. The magnitude and phase of the SAC function has been derived in [13] for Gamma distributed scatterer spacings. Plots of the SAC function magnitude were also presented in [13]. For the extreme case, where the spacing is constant $\Delta_i = \Delta$, substitute $\tau_i = i \Delta$ in (10) to obtain (11) at the bottom of the preceding page.

Equation (11) contains three separate phase factors that affect the coherent sum associated with the spectral peaks. Local maxima form in the bifrequency plane when the complex terms in the double summation are in phase, or coherent. One phase factor results from the complex scatterer responses ($A_n(f) A_m^*(f+\alpha)$) when $n \neq m$. The other two phase factors $e^{-j2\pi f \Delta(n-m)}$ and $e^{j2\pi \alpha \Delta m}$ are associated with the scatterer spacing. The phase relationship denoted by $e^{j2\pi \alpha \Delta m}$ indicates that the coherent sum for the expected value of the SAC function results in spectral peaks along the diagonal elements with $\alpha = n/\Delta$, ($n = \pm 1, 2, 3, \dots$). In addition, the phase relationship denoted by $e^{-j2\pi f \Delta(n-m)}$ results in the location of the spectral peaks along this diagonal, occurring at points where $f = n/\Delta$, ($n = \pm 1, 2, 3, \dots$). The phase term associated with the scattering response between 2 different scatterers can result in degradation of the coherent sum by introducing random phase shifts. As a result the effective scatterer positions (relative to one another) will differ from the actual position and may increase the variance of the scatterer spacings. The effective position due to this additional phase, however, will typically be much less than the axial resolution of the pulse when the acoustic properties of the regular scatterers and surrounding medium are similar for each regular scatterer (Note that Δ will always be greater than or equal to the resolution cell).

The effect of random variations of the scatterer spacing on the SAC function phase is demonstrated for simulated A-scans containing both regular and diffuse echoes. The Gamma distribution used to randomly generate the spacings between regular scatterers is given by

$$f(\Delta; v, \bar{\Delta}) = \frac{(v/\bar{\Delta})e^{-(v\Delta/\bar{\Delta})}(v\Delta/\bar{\Delta})^{v-1}}{(v-1)!} \quad (12)$$

where $\bar{\Delta}$ is the mean scatterer spacing, and v is the order of the Gamma distribution, which is inversely related to the standard deviation of the spacings. The scatterer strengths for both diffuse and regular scatterers were uniformly distributed between 0 and 1, and the regular scatterers were scaled such that a -3 dB ratio existed for the regular-to-diffuse scatterer signal power (see (19)). The rest of the simulator specifications concerning the scatterers and the ultrasonic pulse parameters are presented in Table I.

Since plots of the SAC phase over the bifrequency plane are difficult to interpret visually, one-dimensional phase plots are presented for constant values of α . The phase plots in Fig. 1 result from a simulated A-scan with regularly spaced scatterers 1.02 mm apart and standard deviations of 9.99% and 14.14% for the mean spacing. Fig. 1(a) and (c) plot the phase for $\alpha = 1/\Delta$, while Fig. 1(b) and (d) plot the phase for $\alpha \neq 1/\Delta$. Note the coherency in the plots of the phase

TABLE I
SIMULATOR SPECIFICATIONS

Simulator specifications	Value
Absorption Coefficient	0.94 dB cm ⁻¹
Scattering Coefficient at 180°, measured at 3 MHz	9 x 10 ⁻⁴ Sr ⁻¹ cm ⁻¹
Diffuse Scatterer size	10 μm
Regular Scatterer size	80 μm
Pulse Center Frequency	3.5 MHz
Pulse 3 dB Bandwidth	1.9 MHz
Sampling rate	24 MHz
Propagation velocity	1540 m/s
Mean scatterer spacing	1.02 mm, 2.04 mm

along the diagonal elements of the phase spectrum where $\alpha = 1/\Delta$. The coherent phase is observed in the spectral region from 4 MHz to 8 MHz, where most of the scatterer energy was received. This region represents the upper half of the transducer spectrum, which was skewed upward due to the scatterer size being almost an order of magnitude less than the center frequency wavelength and its interaction with the frequency dependent scattering function. For the phase spectrum where $\alpha \neq 1/\Delta$, the phase plots are incoherent (exhibit wide fluctuations) over the α diagonals. A comparison between Fig. 1(a) and (c) illustrate the deterioration in the coherency of the phase with an increase in the standard deviation of the scatterer distribution.

The coherent phase along the diagonal elements in the bifrequency plane suggests that the averaging involved for frequency smoothing should be applied along the diagonal components of the SAC function. Therefore, in the case of a discrete spectrum, the frequency-smoothing kernel reduces to a diagonal matrix, and (6) becomes a discrete convolution, where the $G_{1/\Delta f}(\cdot)$ is convolved only in the diagonal direction over the bifrequency plane. The optimal shape and width of the frequency-smoothing kernel over several parametric forms are determined using simulations in the next section.

The frequency-smoothed SAC function is normalized over the bifrequency plane to reduce magnitude variations due to system and propagation effects as represented by the factor $H(f; t)H^*(f + \alpha; t)$ in (9). The frequency dependent attenuation resulting from these effects reduces the magnitudes for spectral peaks forming further from the PSD. One form of normalization to reduce this effect is given by

$$P(f, f + \alpha) = \frac{S(f, f + \alpha)}{\sqrt{S(f, f)S(f + \alpha, f + \alpha)}} \quad (13)$$

where $P(\cdot)$ denotes the correlation coefficient. Normalization in this manner scales elements along the PSD diagonal to unity ($\alpha = 0$). All the information regarding scatterer structure is now present along the off-diagonal components of the normalized SAC function. The scatterer spacing is determined by the

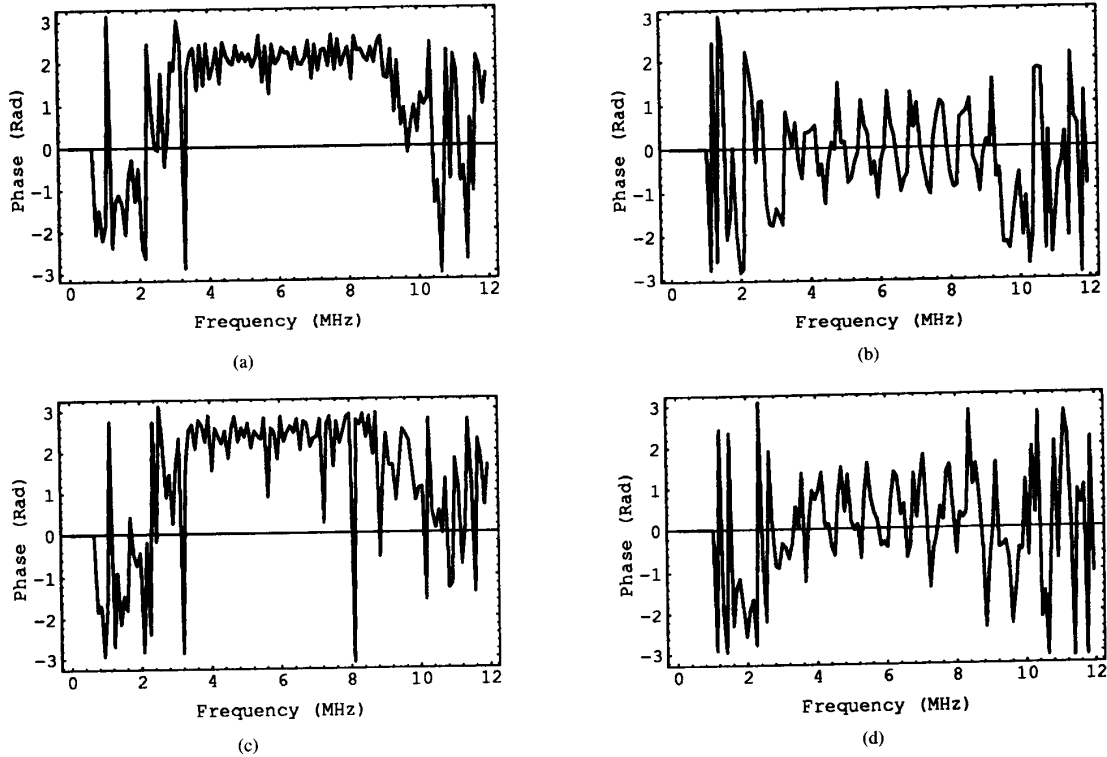


Fig. 1. Phase plots before frequency smoothing for a spacing of 1.02 mm. (a) Standard deviation 0.102 mm (9.99)% and $\alpha = 1/\Delta$. (b) Standard deviation 0.102 mm (9.99)% and $\alpha \neq 1/\Delta$. (c) Standard deviation 0.144 mm (14.14)% and $\alpha = 1/\Delta$. (d) Standard deviation 0.144 mm (14.14)% and $\alpha \neq 1/\Delta$.

dominant peak among the off-diagonal spectral components, which correspond to a frequency distance, $\Delta f = \alpha$, that is used to compute the mean scatterer spacing (see (18)).

Normalization should only be performed over the spectral region where sufficient energy is present (typically the 3 dB to 6 dB range of the PSD) to avoid amplifying regions with low SNR. Spurious peaks often form at the system resolution limit when these regions are included in the normalization. Normalization performed after frequency smoothing results in the magnitude of the low SNR spectral regions being naturally scaled down by the system response so that they do not make a significant contribution in the coherent sum obtained by the frequency smoothing kernel. (Normalizing before frequency smoothing typically scales up the low SNR region in the coherent sum performed by the frequency smoothing kernel.)

By substituting (9) into (13), it can be seen that the scaling factors $H(f;t)H^*(f + \alpha;t)$ cancel out in the magnitude of the normalized quantity. However, the PSD factors in the denominator contain information related to the regular scatterers, since peaks form along the PSD as well as the rest of the bifrequency plane. This actually becomes less of a problem when a strong diffuse component is present, since the diffuse component dominates the PSD in this case. On the other hand when strong regular scatterers exist, sharp peaks form in the PSD, and normalizing before frequency smoothing will scale down the corresponding point in the bifrequency plane more so than its surrounding points. By frequency smoothing the

spectrum before normalization, these sharp peaks along the PSD are smoothed out. This reduces their effect on the height of the off-diagonal peaks.

B. The AR Cepstrum

The AR model is a widely used parametric model in spectral estimation and several efficient algorithms exist for computing AR parameters. The AR model [18] for the sampled sequence $y(n)$ is given by

$$y(n) = - \sum_{k=1}^p a_k y(n-k) + w(n) \quad (14)$$

where $w(n)$ is the input sequence to the system, $y(n)$ is the observed data, a_k 's are the AR parameters and p is the order of the model. If the model order is greater than the number of samples between scatterers, then the PSD associated with the model contains information related to that spacing. For the application of detecting scatterer spacings, if a white noise input is assumed, model order p must be chosen large enough so that the spectrum represented by the AR coefficients can model the quasiperiodic scatterers. Given that $w(n)$ is a stationary random process, the power spectrum of the data can be written as

$$P_Y(f) = |H(f)|^2 P_W(f) \quad (15)$$

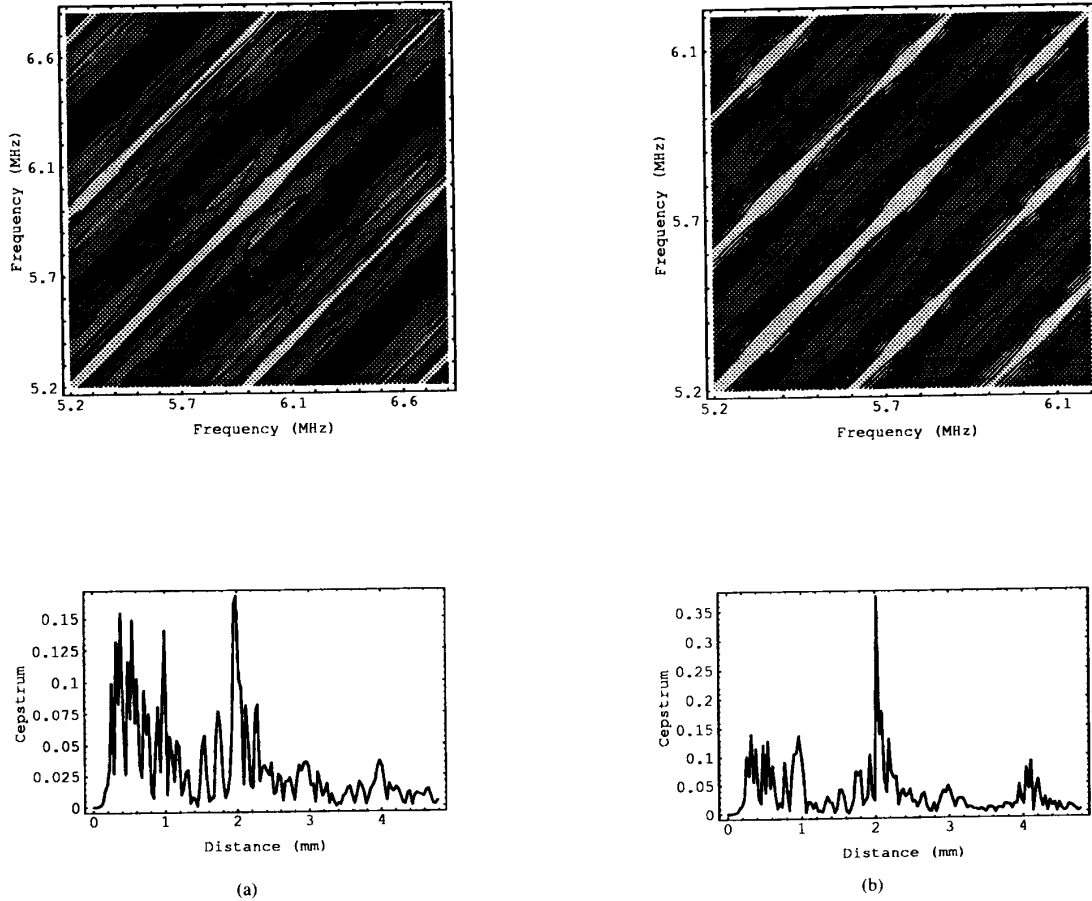


Fig. 2. Frequency-smoothed spectral autocorrelation function and AR Cepstrum for regular scatterers with $\sigma = 3.15\%$ with SNR of -4 dB. (a) 1.02 mm spaced regular scatterers. (b) 2.04 mm spaced regular scatterers.

where $P_W(f)$ is the power spectrum of the input sequence and $H(f)$ is the frequency response of the model. When $w(n)$ is also a zero mean white noise sequence with variance σ_W^2 , the power spectrum of the output sequence is given by

$$P_Y(f) = |H(f)|^2 \sigma_W^2 = \frac{|B(f)|^2 \sigma_W^2}{|A(f)|^2} \quad (16)$$

where for the AR model

$$A(f) = 1 + \sum_{k=1}^p a_p(k) e^{-j2\pi f k}, B(f) = 1. \quad (17)$$

In the model based approach, spectrum estimation consists of two steps. First, the model parameters (a_k) are estimated from the data sequence $y(n)$. Next, the power spectrum is then estimated using (16) and (17). For good results with small data lengths, the order of the AR model is selected in the range $N/3$ to $N/2$ (N is the length of the data segment) [18]. In [8] the order of the AR model was chosen to span a time interval that corresponded to a distance slightly larger than the true scatterer spacing. In this paper the detection of scatterer spacings is considered over a range of values. Thus the AR model order is chosen based on the largest value of the scatterer spacing to be detected.

The mean scatterer spacing is computed from the location of the dominant peak in the cepstrum estimated from the PSD

$$d = \frac{V}{2\Delta f} = \frac{1}{2} V \Delta t. \quad (18)$$

where V denotes the velocity of propagation of the ultrasound pulse, and Δt is the location of the dominant peak in the cepstrum.

The mean scatterer spacing is resolved when the correlation length of the propagating ultrasonic pulse is shorter than the spacing between individual scatterers. The effective resolution of the received echo imposes a limitation on the smallest resolvable scatterer spacing [14]. The largest scatterer spacing determined from the SAC-based estimate is limited by the length of the segment from which the SAC function is computed, while the largest spacing for the AR-based estimate is limited by the AR model order.

III. SIMULATION

Simulation results presented in this section demonstrate the estimation performance of the SAC function in the presence of diffuse backscatter. Simulated A-scans are obtained from (2) and (3). Tissue parameters for the simulation were chosen

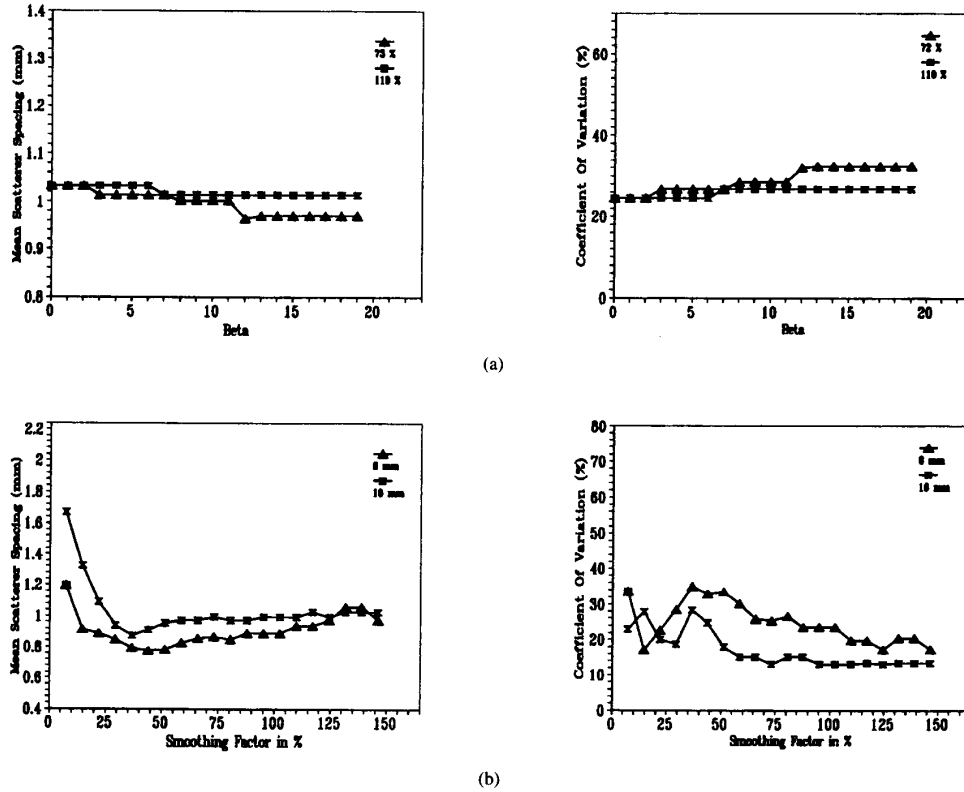


Fig. 3. Mean scatterer spacing and the coefficient of variation for regular scatterers with spacing 1.02 mm and standard deviation 0.144 mm (14.14%). (a) Increasing β to determine an optimum frequency-smoothing kernel shape. (b) Increasing smoothing factor to obtain the optimal spectral width.

within the range of values reported in literature from experimental research with different types of tissue *in vitro* [15]–[17]. Scatterer spacings were simulated from cases with a irregular spacing (standard deviation 14% of mean spacing), to cases with almost deterministic spacings (standard deviation 3% of mean spacing). The standard deviation limits were primarily chosen to observe the performance over an intermediate range. Values for cases of real tissue have been reported by Landini and Verrazzani [6] to range from 10.5% for regular tissue (normal uterus), to 15.8% for intermediate tissue (sclerodal adenosis in breast tissue). Highly disordered tissue (atrophic breast) was considered to have a standard deviation greater than 32%.

The radial positions of the diffuse scatterers were uniformly distributed throughout the beam field of the A-scan, where the number of scatterers were generated with a Poisson distribution (about 15–20 scatterers per resolution cell). The pulse parameters were modified from the initial system response, $h(t)$, to account for the frequency dependent attenuation as the pulse propagated through the tissue. The uniform distribution was used for the scatterer strengths for both regular and diffuse scatterers. The fluctuation in scatterer strength is intended to model changes due to orientation and position of the scatterers within the beam field. In terms of performance, this actually represents the worst case. For distributions with a more central tendency for the regular scatterer strengths (like the Rayleigh

distribution), the performance improves. Table I presents the parameters used in the simulation experiment.

The signal-to-noise ratio between the regular-to-diffuse component was defined as follows:

$$SNR = 10 \log \frac{\int_0^{\Delta t} \left(\sum_{n=1}^{N_S} \int_{-\infty}^{+\infty} h(\tau_n, \tau - \lambda) a_n(\lambda - \tau_n) d\lambda \right)^2 d\tau}{N_S \int_0^{\Delta t} \left(\sum_{n=1}^{N_D} \int_{-\infty}^{+\infty} h(\theta_n, \tau - \lambda) \nu_n(\lambda - \theta_n) d\lambda \right)^2 d\tau} \quad (19)$$

where Δt is the length of the data segment used for frequency smoothing. The simulations vary the SNR by scaling the contributions from the diffuse scattering component (i.e. corresponding to increases and decreases in the diffuse scatterer reflectivity relative to the regular scatterer reflectivity). The factor N_S is included in the denominator to account for the number of regular scatterers over the Δt interval. Without this factor, the SNR would increase with the number of regular scatterers (N_S), rather than be directly related to strength of the scattering functions. In this manner the SNR represents a per-regular-scatterer value independent of their density.

Fig. 2 compares the magnitude plots of the frequency-smoothed SAC function and the AR cepstrum for an A-scan with an SNR (regular-to-diffuse scatterer power) value of -4

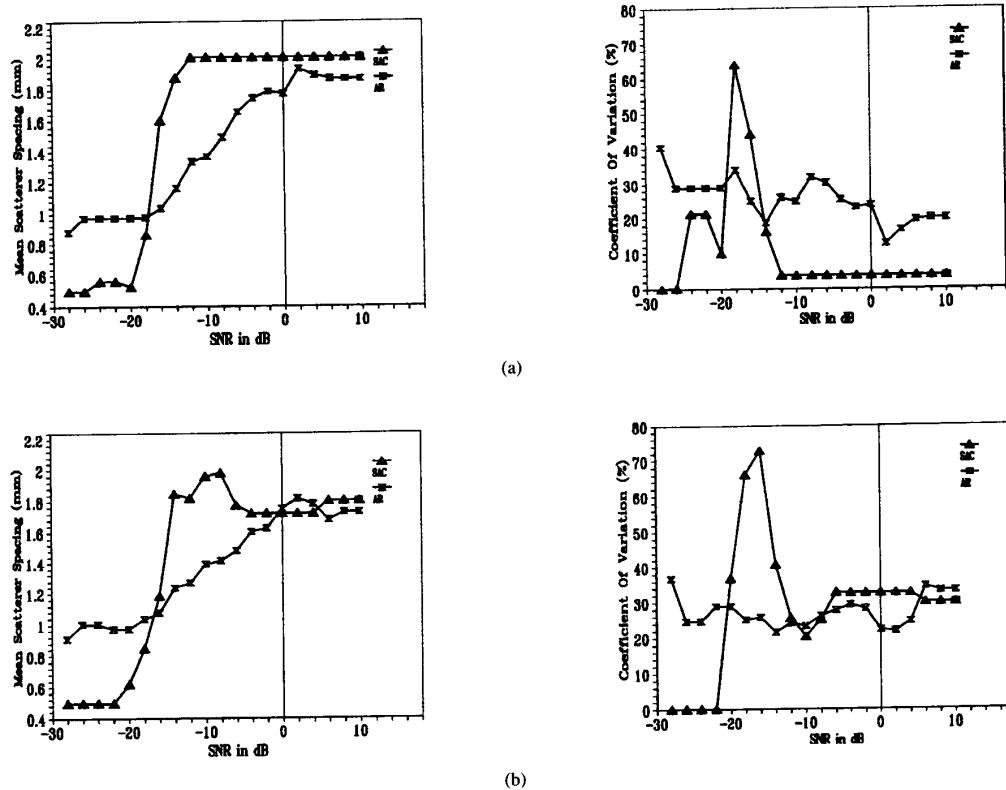


Fig. 4. Mean scatterer spacing and the coefficient of variation for regular scatterers with spacing 2.04 mm for varying SNR values. (a) Standard deviation 0.064 mm (3.15%). (b) Standard deviation 0.204 mm (9.99%).

dB and mean spacings values of 1.02 mm and 2.04 mm, with a standard deviation $\sigma = 3.14\%$. The mean scatterer spacings were chosen to lie on the grid points of the discrete SAC and cepstrum functions. The white bands along the diagonal components (constant α) in the contour plots of Fig. 2 correspond to regions where relative maxima occur in the bifrequency plane. The contour plots were thresholded to truncate the peaking values in the SAC function in order to bring out details over the entire plot, and allow for visual identification of the periodicities. The spectral correlation peak at (6.34, 6.1) MHz in Fig. 2(a) corresponds to a frequency difference $\Delta f = 0.75$ MHz, which by (18), corresponds to a spacing of 1.02 mm. Similarly for Fig. 2(b), the spectral correlation peak at (5.37, 5.75) MHz corresponds to a scatterer spacing of 2.04 mm. As a result of the large noise component, the AR cepstrum exhibits a dominant peak at 2.04 mm in both Fig. 2(a) and (b). The contributions due to the system and the diffuse component are observed as spurious peaks for spacing values smaller than 1 mm. These examples illustrate sensitivity problems associated with the AR cepstrum in the presence of a strong diffuse scattering component.

Mean scatterer spacings for both the AR cepstrum and the SAC function were detected in the range of spacings from 0.4 mm (bandwidth limit of the system) to a spacing of 2.72 mm. To detect scatterer spacings in this range, the AR model requires an order of 70, using the criterion established in [8],

(corresponding to a distance a little larger than 2 mm), and a scaling down of values on the cepstral axis below the 0.4 mm point to reduce the effects of the system response.

Monte-Carlo simulations are used to obtain a quantitative measure of the performance with varying spectral width and shape of the frequency smoothing window. The simulations enable the selection of an optimal frequency smoothing kernel, based on the accuracy of the estimated mean scatterer spacing. Fig. 3 presents the criteria for the selection of the frequency-smoothing kernel shape and width for regular scatterers with a spacing of 1.02 mm, $\sigma = 14.14\%$, and an SNR of -3 dB. The width was denoted in terms of the transducer bandwidth and defined as the smoothing factor, which is the ratio of the frequency-smoothing window size to the bandwidth of the signal (a 4 dB bandwidth was used in the computation of the smoothing factor). All the simulations presented in this paper, were performed over 25 different A-scans. The mean and the coefficient of variation (CV) are computed over the 25 estimates of the mean scatterer spacings. The CV is defined as the ratio of the standard deviation to the mean spacing of the estimated scatterer spacings.

The Kaiser window is used to obtain the optimum kernel shape and is defined as [20]:

$$w[n] = \begin{cases} \frac{I_0[\beta(1 - ((n-\eta)/\eta)^2)^{1/2}]}{I_0(\beta)}, & 0 \leq n \leq M \\ 0 & \text{elsewhere} \end{cases} \quad (20)$$

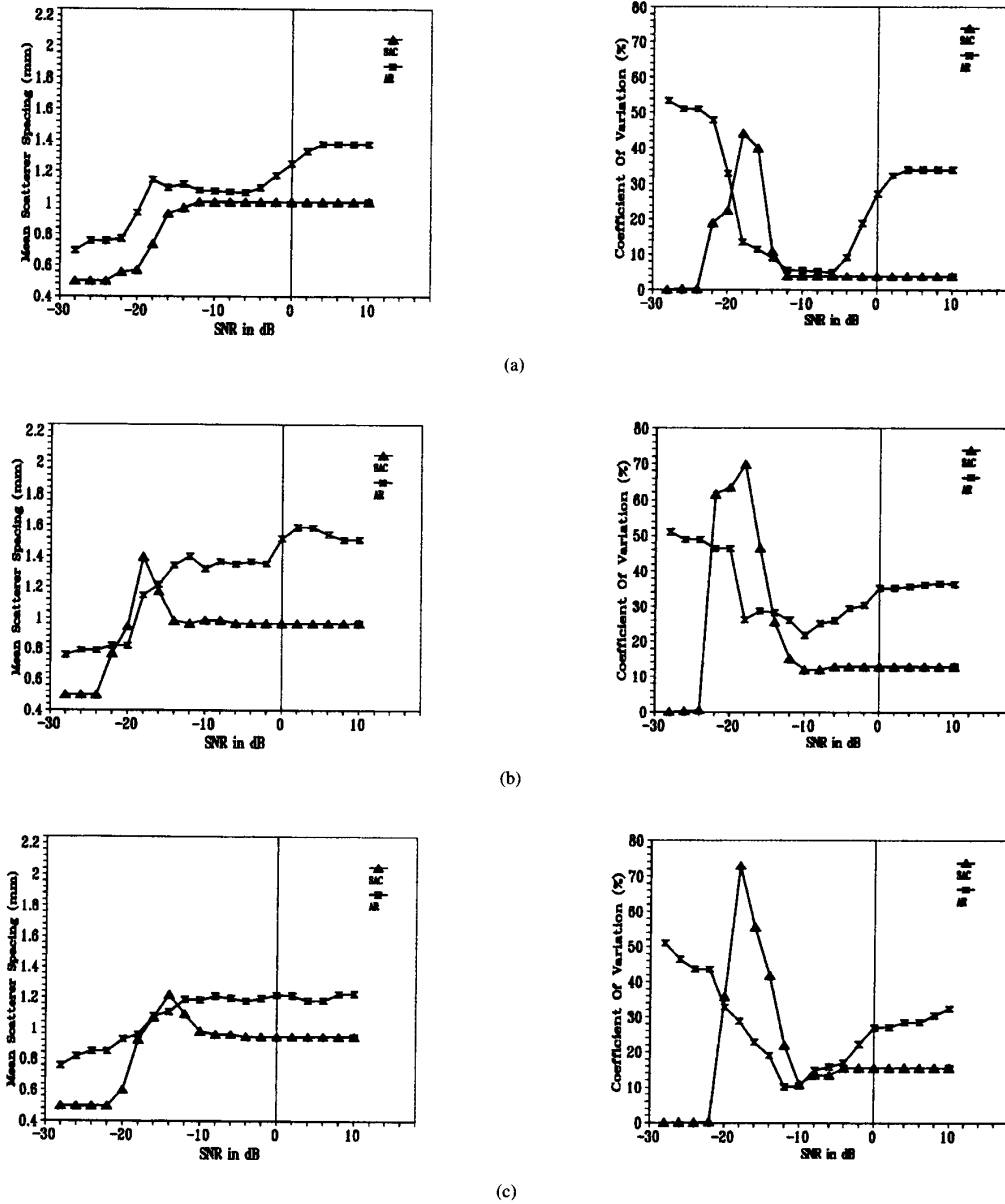


Fig. 5. Mean scatterer spacing and the coefficient of variation for regular scatterers with spacing 1.02 mm for varying SNR values. (a) Standard deviation 0.032 mm (3.15)%. (b) Standard deviation 0.102 mm (9.99)%. (c) Standard deviation 0.144 mm (14.14)%.

where $\eta = M/2$, and $I_0(\cdot)$ represents the zeroth-order modified Bessel function of the first kind. The Kaiser window is defined by two parameters, the length $(M+1)$ and the shape parameter β . The window length and shape can be varied to obtain the desired sidelobe amplitude or mainlobe width by varying these two parameters. For $\beta = 0$, the Kaiser window reduces to a rectangular window and increasing values of β approximates a window which emphasizes the spectral components at the center of the window (Bartlett window with $\beta = 1.33$, Hamming window with $\beta = 4.86$, Blackman window with $\beta = 7.04$). Fig. 3(a) compares the performance

of the mean scatterer spacing estimator for two values of the smoothing factor for β ranging from 0 to 20. Note, from Fig. 3(a), for β values less than 3, the mean scatterer spacing estimated is more accurate and has the smallest CV. However, from Fig. 3(a), it is apparent that the shape of the frequency-smoothing window does not significantly impact the performance of the spacing estimator.

Selection of the frequency-smoothing kernel width was thus made using a square window (all ones along the diagonal). Fig. 3(b) shows plots of the mean scatterer spacing and CV plotted as a function of the smoothing factor. The simulations

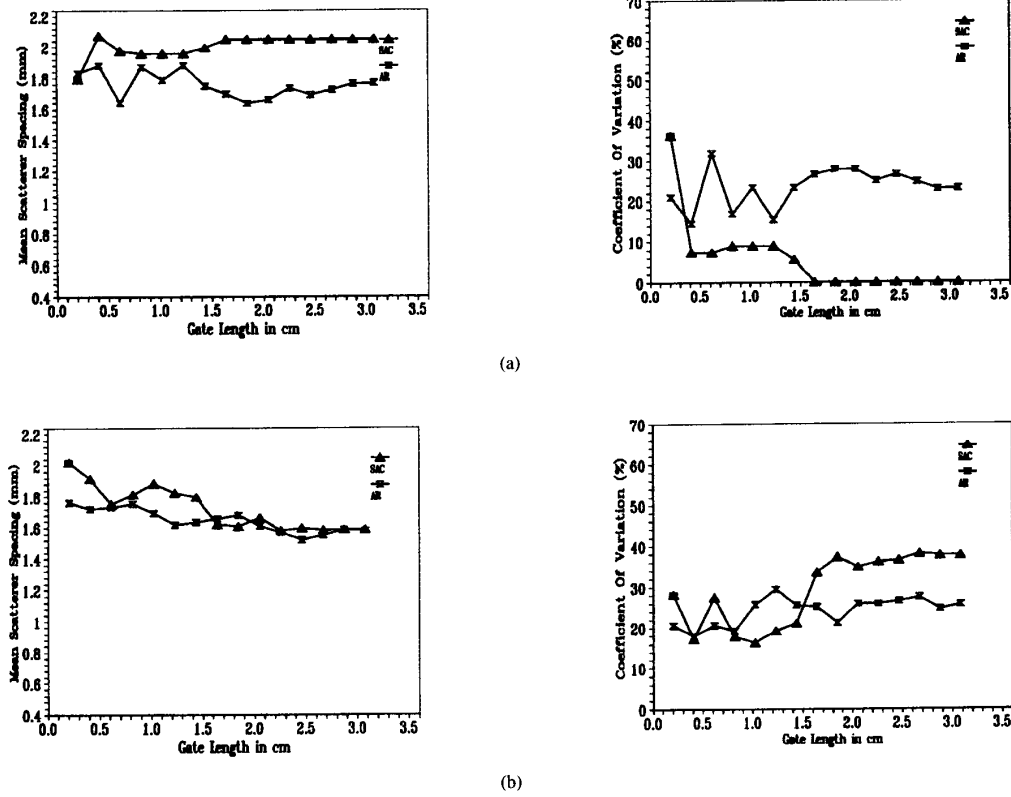


Fig. 6. Mean scatterer spacing and the coefficient of variation for regular scatterers with spacing 2.04 mm for varying gate lengths. (a) Standard deviation 0.064 mm (3.15%). (b) Standard deviation 0.204 mm (9.99%).

were performed for data segments with lengths 8 mm and 16 mm. The plots show convergence of the mean scatterer spacing to its true value from about 75% with $\sigma = 14.14\%$. The larger number of regular scatterers in the longer data segment cause the correlation peaks to retain their coherence when compared to the smaller 8 mm data segment. This is observed in Fig. 3(b), where the scatterer spacing estimate detected from the 16 mm data segment is more accurate and has lower CV.

Simulations were performed for a data segment of length 16 mm (corresponding to 512 discrete points with the sampling frequency of 24 MHz), and a smoothing factor of 87% for the SAC function. Simulation results are presented for mean scatterer spacings of 1.02 mm and 2.04 mm. Since larger scatterer spacings in the A-scan cause the formation of spectral correlation peaks closer to the PSD, the 2.04 mm spacing (about 7–8 scatterers) illustrates the performance of the SAC function in this region. Critical sources of degradation in this region result from spectral leakage from the PSD into the bifrequency plane, and the smaller number of scatterers, which contribute to the phase coherence in the spectral correlation peaks. As a result, the phase coherence along constant α closer to the PSD degrades more rapidly with an increase in the standard deviation in the scatterer spacing. For spectral peaks further away from the PSD, the contributions due to spectral leakage reduce. However, as the peak occurs further

away from the PSD, the contributing frequencies approach the band-width limit of the system, which is characterized by lower SNR. The 1.02 mm spacing illustrates performance as this region is approached.

The performance of the scatterer spacing estimators as a function of SNR is shown in Figs. 4 and 5. The mean spacing and the CV are presented for SNR values ranging from -30 dB to 10 dB. The SAC function reliably detects the regular 2.04 mm scatterer spacing down to an SNR of about -12 dB, as observed in Fig. 4(a) with $\sigma = 3.14\%$. The cepstral technique using the AR model detects the 2.04 mm scatterer spacing for SNR values greater than 2 dB with a small bias of 0.14 mm for $\sigma = 3.14\%$. When σ is increased to 9.99%, the mean spacing estimate for either method does not converge, as observed in the CV plot (Fig. 4(b)). At low SNR (less than -20 dB) the SAC function estimate converges to the resolution limit (0.4 mm) of the system. A maximum occurs consistently in the SAC function at the resolution limit when no detectable scatterer spacing exists in the data segment.

Fig. 5 presents the performance of the SAC function for the 1.02 mm spacing. A comparison between Figs. 4 and 5 shows that a more accurate scatterer spacing estimate can be obtained for the 1.02 mm spacing even for large σ (see Fig. 5(b) and (c)). The cepstral technique using the AR model, however, does not reliably detect the 1.02 mm scatterer spacing as

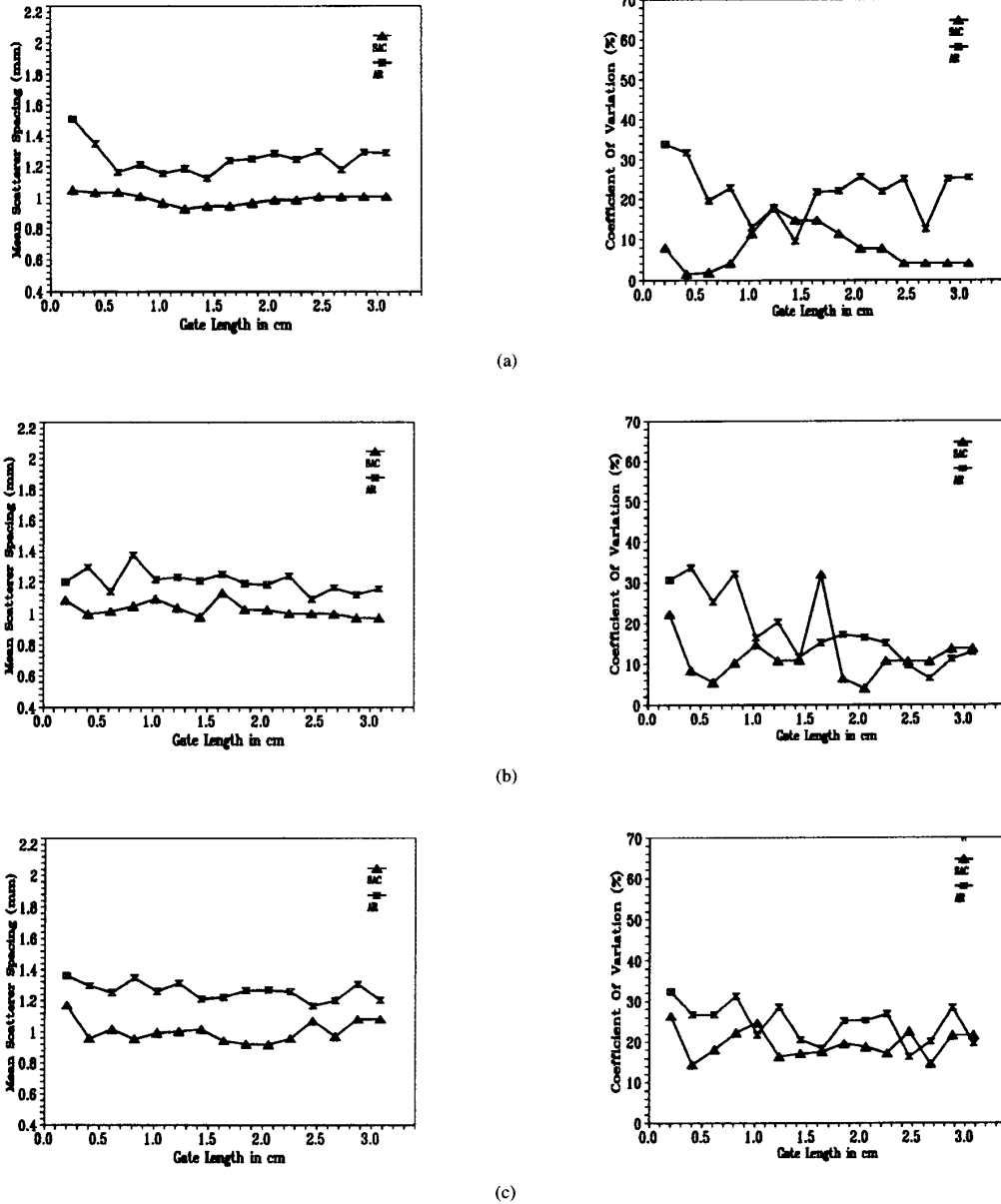


Fig. 7. Mean scatterer spacing and the coefficient of variation for regular scatterers with spacing 1.02 mm for varying gate lengths. (a) Standard deviation 0.032 mm (3.15%). (b) Standard deviation 0.102 mm (9.99%). (c) Standard deviation 0.144 mm (14.14%).

observed in the CV of Fig. 5(a)–(c). The CV for the SAC, on the other hand, appears to closely follow the standard deviation of the regular scatterer spacings in the A-scans for SNR values greater than -10 dB.

Performance comparisons with an SNR of -3 dB are illustrated in Figs. 6 and 7 for increasing gate lengths. The estimates obtained using the SAC function for the 2.04 mm spacing converge reliably for $\sigma = 3.14\%$ as shown in Fig. 6(a), however, the performance degrades significantly for $\sigma = 9.99\%$ as seen in the CV plots (CV = 35%). For the 1.02 mm spacing with $\sigma = 3.14\%$ (Fig. 7(a)), the estimated spacing

converges to the true scatterer spacing within 2 cm with a CV of 4% and performs reliably even for large σ (Fig. 7(b) and (c)).

The AR model performs poorly in the estimation of both the 1.02 mm and the 2.04 mm spacings as seen for $\sigma = 3.14\%$ (Figs. 6 and 7(a)). The low value of the SNR (-3 dB) leads to the occurrence of more spurious peaks resulting in a CV of about 25% for the cases shown in Fig. 7. In addition, a bias also exists for the AR estimate. As observed in Fig. 2, there is a tendency for the cepstrum to have a peak at 2 mm, which results in the erratic behavior of the AR cepstrum spacing

estimator. In the case of the 2.04 mm scatterer spacing, the major contributor to the poor performance of the AR technique was the low value of the SNR, which increases the diffuse component leakage into the detection range of the cepstral axis.

IV. EXPERIMENTAL RESULTS

In this section data from *in vivo* scans of liver tissue are provided as an example for estimating the mean scatterer spacing using the SAC function and AR cepstral analysis. B-scan images of the liver were obtained using the Ultramark 9 ultrasound system (ATL, Bothell, WA). The individual RF A-scans were directly obtained from this system using a transducer with a center frequency $f_c = 3.5$ MHz, 3 dB bandwidth $f_{3\text{ dB}} = 2.0$ MHz, and a sampling frequency $f_s = 12$ MHz. An anti-aliasing filter with a cutoff frequency of 6 MHz was applied to each A-scan before sampling.

Normalized magnitude plots of the frequency-smoothed SAC function, AR cepstrum, and the liver tissue A-scan segment are presented in Fig. 8. The A-scan segment for liver tissue shows the presence of a mean scatterer spacing near 1 mm. Vertical lines are drawn through the A-scan to draw attention to points where local maxima exist. These were determined visually and represent a rough approximation. The SAC function and the AR cepstrum were obtained from the single data segment of 8 mm. The light shaded bands along the diagonal components in the contour plots of Fig. 8(b), correspond to regions where relative maxima occur in the bifrequency plane. The spectral components along the diagonal with $\alpha = 2.65$ MHz indicates a frequency difference $\Delta f = (2.65 - 1.9)$ MHz = 0.75 MHz, which corresponds to a spacing value of 1.02 mm for the SAC function. The AR cepstrum detects a spacing value near 0.6 mm as observed from the cepstral peak in Fig. 8(c), which is close to the resolution limit of the system and is most likely due to leakage from the diffuse component.

This section presented an application of the SAC function to reveal the regular structure of human liver tissue. The extra information provided by the coherent phase terms results in the spectral peaks being more pronounced in the SAC function, and the subsequent reduction in the effect of diffuse scattering. The cepstrum on the other hand did not exploit this phase information, and was more susceptible to spurious peaks due to the presence of the diffuse component.

V. CONCLUSION

This paper introduced the frequency-smoothed SAC function for estimating the mean scatterer spacing. The SAC function technique was compared to a cepstral technique using an AR model (based on Burg's algorithm). The SAC function is shown to estimate the mean scatterer spacing more reliably than the cepstral technique in the presence of strong diffuse scattering.

For cepstral techniques, the selection of a cutoff value along the axis to reduce the system effects and reveal the tissue signature determines the minimum detectable scatterer spacing. The cutoff value should be set at the resolution limit of the

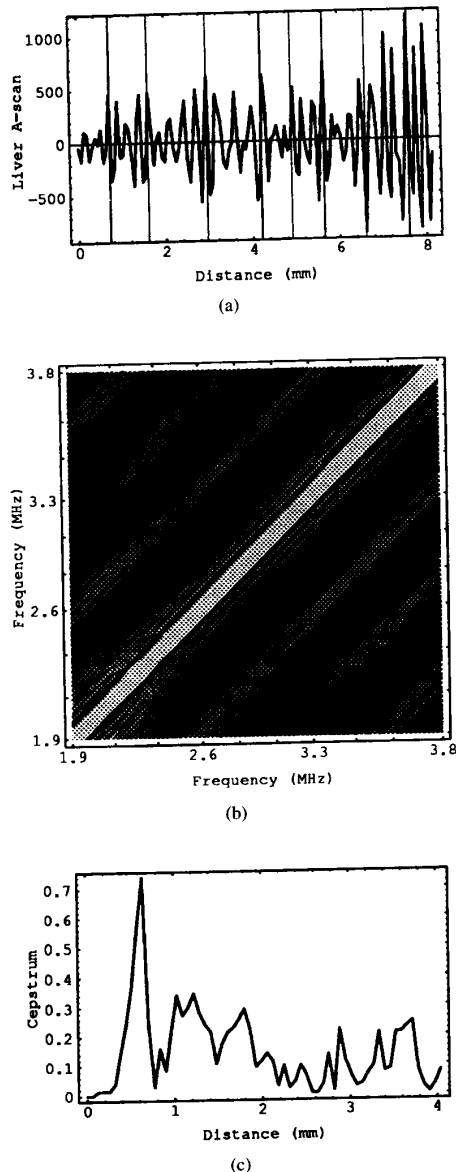


Fig. 8. (a) A-scan segment for liver tissue. (b) Frequency-smoothed SAC function and, (c) AR Cepstrum for the A-scan segment of liver tissue.

system to avoid the detection of spurious periodicities below the system limit. In addition, the order of the AR model has to be specified, which determines the largest spacing detectable by this method. The SAC function provides a reliable and robust technique of estimating the scatterer spacing. However, normalizing the SAC function requires that information be taken only from the spectral region of the imaging system with sufficient energy above that of system noise. The limit on the spectral range limits the minimum detectable scatterer spacing for the SAC function.

Frequency smoothing can be used to obtain a statistical spectrum over smaller data segments when compared to time-averaging. Frequency smoothing can therefore be used in cases

where the scatterer spacing is stationary over comparably short intervals relative to that for time-averaging. For quasiperiodic scatterers the mean scatterer spacing estimate improves with an increase in the number of regular scatterers within the data segment as they contribute to the phase coherence. The SAC function provides an estimation technique that is more reliable than PSD based techniques, due to the utilization of the phase relationship between the regular resolvable scatterers.

This work does not examine the effects of two-dimensional distributions of regular scatterers, which is of practical interest especially for systems with wide beam fields. In some cases the radial distances between the regular scatterers over a two or three dimensional region may not be regular, and the resulting A-scan will not exhibit the quasiperiodic spacing as shown in the liver scan presented in this paper. Thus, in most cases the scatterer spacings estimates should be used with focused transducers, where the dominant scattering process is close to the A-scan axis. This work also considers only long range order (due to portal triads in liver tissue) in the distribution of the regular scatterers. The technique presented in this paper, however, can be used to characterize tissues with short range order (resolvable blood vessels), but a higher SNR than that reported for long range order would be required.

ACKNOWLEDGMENT

The authors would like to thank the Division of Ultrasound at the Thomas Jefferson University Hospital for collecting the experimental data used in this paper. The authors would also like to thank the reviewers for their suggestions that significantly improved the content and clarity of the paper.

REFERENCES

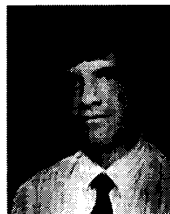
- [1] M. F. Insana, R. F. Wagner, D. G. Brown, and T. J. Hall, "Describing small-scale structure in random media using pulse-echo ultrasound," *J. Acoust. Soc. Am.*, vol. 87, pp. 179-192, Jan. 1990.
- [2] L. L. Fellingham and P. G. Sommer, "Ultrasonic characterization of tissue structure in the *in vivo* human liver and spleen," *IEEE Trans. Son. Ultrason.*, vol. 31, pp. 418-428, July 1984.
- [3] B. S. Garra, M. F. Insana, T. H. Shawker, R. F. Wagner, M. Bradford, and M. Russell, "Quantitative ultrasonic detection and classification of diffuse liver disease," *Invest. Radiol.*, vol. 24, no. 3, pp. 196-203, Mar. 1989.
- [4] R. F. Wagner, M. F. Insana, and D. G. Brown, "Unified approach to the detection and classification of speckle texture in diagnostic ultrasound," *Opt. Eng.*, vol. 25, no. 6, pp. 738-742, June 1986.
- [5] M. F. Insana, R. F. Wagner, B. S. Garra, D. G. Brown, and T. H. Shawker, "Analysis of ultrasound image texture via generalized Rician statistics," *Opt. Eng.*, vol. 25, no. 6, pp. 743-748, June 1986.
- [6] L. Landini and L. Verrazzani, "Spectral characterization of tissue microstructure by ultrasound: A stochastic approach," *IEEE Trans. Ultrason. Ferroelect. Freq. Cont.*, vol. 37, pp. 448-456, Sept. 1990.
- [7] R. Kuc, K. Haghkerder, and M. O'Donnell, "Presence of cepstral peaks in random reflected ultrasound signal," *Ultrason. Imaging*, vol. 8, pp. 196-212, July 1986.
- [8] K. A. Wear, R. F. Wagner, M. F. Insana, and T. J. Hall, "Application of auto-regressive spectral analysis to cepstral estimation of mean scatterer spacing," *IEEE Trans. Ultrason. Ferroelect. Freq. Cont.*, vol. 40, pp. 50-59, Jan. 1993.
- [9] W. A. Gardner, "Exploitation of spectral redundancy in cyclostationary signals," *IEEE Signal Proc. Mag.*, vol. 8, pp. 14-36, Apr. 1991.
- [10] K. D. Donohue and T. Varghese, "Spectral cross-correlation for tissue characterization," in *IEEE Ultrason. Symp.*, 1992, vol. 2, pp. 1049-1052.
- [11] T. Varghese and K. D. Donohue, "Characterization of tissue microstructure scatterer distribution with spectral correlation," *Ultrasound Imaging*, vol. 15, pp. 238-254, July 1993.
- [12] T. Varghese and K. D. Donohue, "Mean scatterer spacing estimates with spectral correlation," *J. Acoust. Soc. Amer.*, vol. 96, no. 6, pp. 3504-3515, Dec. 1994.
- [13] K. D. Donohue, J. M. Bressler, T. Varghese, and N. M. Bilgutay, "Spectral correlation in ultrasonic pulse-echo signal processing," *IEEE Trans. Ultrason. Ferroelect. Freq. Cont.*, vol. 40, pp. 330-337, July 1993.
- [14] K. D. Donohue, T. Varghese, and N. M. Bilgutay, "Spectral redundancy in characterizing scatterer structures from ultrasonic echoes," in *Review of Prog. Quant. Nondest. Eval.*, D.O. Thompson, and D. E. Chimenti, Eds. New York: Plenum Press, 1994, p. 13.
- [15] L. R. Romijn, J. M. Thijssen, and G. W. J. Van Beuning, "Estimation of scatterer size from backscattered ultrasound: A simulation study," *IEEE Trans. Ultrason. Ferroelect. Freq. Cont.*, vol. 36, pp. 593-605, Nov. 1989.
- [16] J. C. Bamber, "Theoretical modeling of the acoustic scattering structure of human liver," *Acoust. Lett.*, vol. 3, pp. 114-119, 1979.
- [17] D. Nicholas, "Evaluation of backscattering coefficients for excised human tissue: results, interpretation and associated measurements," *Ultrasound Med. Bio.*, vol. 8, pp. 17-28, Aug. 1982.
- [18] J. G. Proakis and D. G. Manolakis, *Digital signal processing, Principles, Algorithms and Applications*. New York: Macmillan, 1992.
- [19] A. Papoulis, *Probability, Random Variables and Stochastic Processes*. New York: McGraw Hill, 1991.
- [20] A. V. Oppenheim and R. W. Schaffer, *Discrete-Time Signal Processing*. Englewood Cliffs, NJ: Prentice Hall, 1989.



Tomy Varghese (S'92) received the B.E. degree in Instrumental Technology from the University of Mysore, India, in 1988, and the M.S. degree in electrical engineering from the University of Kentucky, Lexington, KY in 1992. He is currently working towards the Ph.D. degree at the University of Kentucky.

From 1988 to 1990 he was employed as an Engineer in Wipro Information Technology Ltd., India. His current research interests include detection and estimation theory, statistical pattern recognition, and signal and image processing applications in medical imaging.

Mr. Varghese is a Student Member of IEEE and a Member of Eta Kappa Nu.



Kevin D. Donohue (S'84-M'87) received the B.A. degree in mathematics from Northeastern Illinois University, Chicago, IL, in 1981, and the B.S., M.S., and Ph.D. degrees from the Illinois Institute of Technology, Chicago, IL, in 1984, 1985, and 1987, respectively.

In 1985, Dr. Donohue was an Engineer for Zenith Electronics, in Glenview, IL, developing ultrasonic detection circuits. From 1989 to 1991 he was a Visiting Assistant Professor at Drexel University doing research in radar and ultrasonic signal detection. He is currently an Associate Professor in the Electrical Engineering Department at the University of Kentucky. His current research interests include detection and estimation theory, spectral estimation, statistical signal processing, and image processing for applications in nondestructive testing of materials and medical imaging.

Dr. Donohue is a Member of IEEE and Sigma Xi.